

University of Wisconsin – Madison

Simultaneous Assessment of Axonal Density and Cerebrovascular Disease in Alzheimer's Disease using 4D Flow MRI and Neurite Orientation Dispersity and Density Imaging

Authors: Grant S. Roberts

Class: MP/NTP 651

Date: 12/07/2020

Abstract:

It has been observed that white matter (WM) alterations occur in a majority of patients with Alzheimer's disease (AD). It is hypothesized that such alterations may, to some extent, be the result of cerebrovascular disease (CVD). However, it is unclear the degree to which CVD influences WM at the microstructural level. In this study, the effects of CVD on microstructural changes were assessed in a cohort of 20 AD and 41 healthy, cognitively normal (CN) subjects using 4D flow MRI and neurite orientation dispersion and density imaging (NODDI). A NODDI processing pipeline was developed in FSL and MATLAB from multi-shell diffusion tensor imaging (DTI) data in order to produce neurite density index (NDI) maps. Whole-brain voxel-wise group differences in NDI values were explored using tract-based spatial statistics (TBSS). Furthermore, correlations between CVD metrics – specifically pulse wave velocity (PWV), pulsatility index (PI), and total cerebral blood flow (tCBF) – and NDI between AD and CN groups were also explored. Significant clusters were associated with WM tracts using pre-labelled WM atlas; these clusters were then analyzed post hoc using a region of interest (ROI)-based analysis. Analysis of covariance (ANCOVA) tested differences in NDI between CN and AD groups in ROIs, after adjusting for both age and sex. Subsequently, correlations between NDI and CVD metrics, as well as differences in correlation between AD and CN groups, were tested using fixed-effect linear regression models. TBSS demonstrated significant differences in NDI between groups in multiple tracts. Individualized post hoc ROI analysis verified these findings in the corpus callosum, corona radiata, posterior thalamic radiation, external capsule, cingulum, cingulate cortex, superior longitudinal fasciculus, and uncinate fasciculus. TBSS revealed some areas of negative correlations between PI and NDI in the CN group. Upon performing ROI analysis in regions where PI and NDI were negatively correlated, there were no significant correlations after correcting for multiple comparison. There were a number of regions with positive correlations between tCBF and NDI in the CN group. ROI analysis demonstrated many significant areas of positive tCBF and NDI correlation, however, only the superior longitudinal fasciculus survived multiple comparisons. These results support findings from other studies of similar scope, demonstrating differences in NDI between CN and AD groups in many subcortical structures. Additionally, only correlations between tCBF and NDI were observed, suggesting that blood flow may be an important factor in WM degeneration. Further studies assessing NDI changes in individuals with mild cognitive impairment are warranted to study the effects of cerebral blood flow in WM degeneration in the preclinical AD stage.

Introduction:

Alzheimer's disease (AD) is an irreversible, neurodegenerative disease which causes brain atrophy and progressive worsening of cognition. AD is typically considered to be a disease of gray matter, primarily due to the spatial distribution of neuronal cell death caused by extracellular beta-amyloid (A β) accumulations and intracellular neurofibrillary tangles¹. A great deal of focus has thus been devoted to assessing cortical atrophy^{2,3}, gray matter microstructural alterations⁴, and detecting presence of A β and tau proteins in gray matter⁵. However, white matter (WM) alterations are also known to occur in individuals with AD^{6,7} and may even precede gray matter degeneration^{8,9}, suggesting that WM damage is not a secondary process to damage of gray matter. Large scale WM alterations can often be visualized on diagnostic images as white matter hyperintensities¹⁰, which have been shown to be strong predictors of AD and dementia¹¹. While there have been a number of studies assessing macroscopic WM alterations in AD cohorts, there have been only a handful of studies assessing initial alterations at the level of the tissue microstructure¹²⁻¹⁸. However, these studies have shown that demyelination and decreased axonal densities occur in various subcortical structures in individuals with AD.

It has been hypothesized that microstructural WM degeneration is, to some extent, the result of microvascular injury^{19,20}. According to the two-hit hypothesis presented by Zlokovic, cardiovascular and cerebrovascular disruptions lead to damage in the brain's microcirculation, which then leads to subsequent vascular-mediated neuronal dysfunction and impaired drainage of A β ²¹. This hypothesis is further supported from recent findings that indicate that blood-brain barrier dysfunction²²⁻²⁴, hypoperfusion²⁵⁻²⁷, altered cerebrovascular hemodynamics²⁸⁻³⁰, and various cardiovascular risk factors³¹⁻³⁴ are associated with AD progression and may even precede amyloid deposition. It is thus plausible that vascular disease and amyloid deposition are synergistically involved in Alzheimer's disease³⁵. Importantly, there have been no studies to date that have simultaneously assessed the relationship between WM microstructural damage and cerebrovascular health. Studying this relationship has been partly limited by the lack of sufficiently sensitive tools to evaluate vascular and microstructural pathology; however, novel imaging techniques have now made this analysis possible.

Magnetic resonance imaging (MRI) is a particularly sensitive, non-invasive imaging modality capable of capturing morphological tissue properties, diffusion of water, and blood flow. Novel methodologies have been developed for the comprehensive assessment of cerebrovascular hemodynamics, for instance, time-resolved, volumetric, velocimetry measurements (4D flow MRI^{36,37}). Our research group has previously used an accelerated, radially-

undersampled 4D flow MRI acquisition to identify differences in mean blood flow^{28,34,38}, pulsatility^{29,39,40}, and pulse wave velocities⁴¹ between AD, mild cognitively impaired (MCI), and age-matched control subjects. Recently, a novel technique termed neuroite orientation dispersion and density imaging (NODDI) has been introduced as a method to probe cerebral microstructure on a voxel-wise basis⁴². NODDI works by fitting data from a multi-shell diffusion tensor imaging (DTI) acquisition into an *a priori* three-compartment tissue model, allowing for robust measurements of orientation dispersion indices (ODI), neuronal density indices (NDI), and volume fraction of isotropic water molecules (V_{iso})⁴³.

The aim of this study is to develop a NODDI processing pipeline using multi-shell diffusion tensor imaging (DTI) data in order to analyze NDI, a surrogate measure for WM axonal density, in 20 AD subjects and 41 cognitively normal (CN) age-matched individuals. Using tract-based spatial statistics (TBSS), associations between WM axonal degeneration and cerebrovascular health metrics will be explored between AD and control groups. It is hypothesized that (1) NDI values will be significantly different between both groups in WM tracts that are known to be affected by AD and (2) altered macroscopic cerebrovascular hemodynamics will be correlated with decreased NDI metrics in regions where WM alterations have been observed. The capabilities of simultaneously assessing vascular disease and structural brain changes allow for a better understanding of the potentially synergistic or causative role that vascular disease plays in AD progression. Additionally, such knowledge may assist in the future development of novel imaging biomarkers to diagnose AD in the preclinical stage.

Materials and Methods:

4D Flow MRI – Theory

4D flow magnetic resonance imaging (MRI) allows for the acquisition of 3D, time-resolved, velocity fields encoded in each of the 3 Cartesian directions⁴⁴. In other words, at each voxel within a given 4D flow volumetric dataset, there exists an associated 3D velocity vector relating to a spin's motion in the x-, y-, and z-directions. Because cardiac gating is applied, there are often multiple volumes representing data at various points along the cardiac cycle. 4D flow MRI is a phase contrast (PC) technique in which velocity encoding gradients are used to encode velocity into the *phase* of the complex-valued MRI signal. Moving spins will acquire a deterministic phase shift depending on their speed relative to the direction of the encoding gradient, while non-moving spins will theoretically acquire no phase shift. This is described by Equation 1:

$$\phi(\vec{r}, TE) = \phi_0 + \gamma \cdot \vec{r}_0 \int_0^{TE} \vec{G}(t) \cdot dt + \gamma \cdot \vec{v} \int_0^{TE} \vec{G}(t)t \cdot dt + \dots \quad (1)$$

where \vec{r} is the time-dependent position of a given spin, TE is the echo time, ϕ is the resultant image phase, ϕ_0 is the background phase, γ is the gyromagnetic ratio of hydrogen (42.58 MHz/T), \vec{r}_0 is the initial spin position, \vec{v} is the velocity of a given spin at position \vec{r}_0 , and $\vec{G}(t)$ describes the (typically bipolar) gradient waveform⁴⁵. Note higher orders of motion are often excluded, but can result in displacement artifacts if spins exhibit acceleration, jerk, etc. However, discussion of this topic is out of the scope of this paper (see papers by Frayne et al.⁴⁶ and Steinman et al.⁴⁷ for further details). In a practical setting, stationary spins will still acquire some phase shift due to field inhomogeneities. Because of this, it is common to acquire an additional “reference” scan with no encoding gradients to account for background phase shifts in stationary spins. Many standard 4D flow sequences utilize 4-point encoding to encode velocity in 3 directions and acquire an additional reference scan⁴⁸. However, higher-order encoding schemes can be used to increase signal-to-noise ratio (SNR) and velocity-to-noise ratio (VNR)⁴⁹.

4D flow data can be used to study intravascular hemodynamics over a time-averaged heartbeat, useful in quantifying systolic/diastolic blood velocities, volumetric blood flow rates, pulsatility, wall shear stress, pulse wave velocities, and many other parameters⁵⁰. Additionally, due to the inherent contrast between moving spins (inside vessels) and stationary spins (background), high-quality angiograms can be simultaneously generated from the data⁵¹. Thus, 4D flow MRI can provide both morphological information (PC angiogram) and quantitative flow data through data post-processing. Due to the high-dimensionality of 4D flow data, advanced reconstruction algorithms and accelerated imaging techniques must be used to obtain data in clinically feasible scan times. For this study, we utilize a radially-undersampled sequence, termed PCVIPR (Phase Contrast, Vastly-Undersampled Isotropic Projection Reconstruction)³⁷. The radial sampling scheme offers several advantages over Cartesian acquisitions including: higher spatial resolution capabilities, improved robustness to motion artifacts by oversampling central k-space⁵², favorable noise properties for parallel imaging and regularized reconstructions⁵³, and flexible retrospective gating schemes⁵⁴. Advanced reconstruction methods have also been used to further accelerate imaging or to increase data fidelity⁵⁵. A recent paper by Rivera-Rivera et al. demonstrated the feasibility of using a locally low rank reconstruction and flow encode splitting to obtain ultra-high temporal resolution 4D flow data for the use of computing intracranial pulse wave velocities⁴¹. Pulse wave velocity (PWV) describes the rate at which pulse pressure propagates through a vessel and is clinically important because it indirectly relates to arterial stiffness, which increases as cardiovascular disease progresses⁵⁶. Additionally, the pulsatility index (PI), defined as the difference between the systolic and diastolic velocities normalized by the

mean velocity, can also provide surrogate measure for vascular disease⁵⁷. PI and PWV data, as well as total cerebral blood flow (tCBF) measures, have already been obtained for every patient in this study. This analysis was conducted by Rivera-Rivera et al. for a separate study and will be used in this study as indirect measures of cerebrovascular health.

NODDI – Theory

Diffusion tensor imaging (DTI) is a powerful application of MRI, capable of characterizing the diffusion of water molecules *in vivo*. Diffusion describes the random displacement of particles (e.g. water) over time. For free water, diffusion can be statistically modelled as a Gaussian distribution which is a function of space, time, and a physical constant known as the diffusion coefficient (describing the ease with which molecules diffuse). Using diffusion weighted imaging (DWI), bipolar diffusion gradients (similar to those used in phase contrast imaging) can be utilized to sensitize MR signal to diffusion. Specifically, for voxels with high degrees of perfusion, water molecules will dephase as they move along the bipolar diffusion gradient. This will then lead to an incoherence in the phase of the spins, which leads to a decrease in signal. Conversely, in areas with low degrees of perfusion, water molecules will be mostly stationary and thus will dephase less while the diffusion gradients are turned on, leading to a higher MR signal. In addition to diffusion, the degree of spin dephasing is also dependent on the timing and strength of the bipolar gradients. This dependency can be described by a “b-value”, which is governed by Equation 2:

$$b = \gamma^2 G^2 \delta^2 \left(\Delta - \frac{\delta}{3} \right) \quad (2)$$

where γ is the gyromagnetic ratio of hydrogen (42.58 MHz/T), G is the gradient strength, δ is the on-time for one pole of the diffusion gradient, and Δ is the time between the start of the first pole and start of the second pole of the bipolar gradient. Using Equation 2, the signal after applying diffusion gradients is given by Equation 3:

$$S = S_0 e^{-b \cdot ADC} \quad (3)$$

Here, S represents the relative image signal, S_0 is the image signal with no gradients applied, and ADC is the apparent diffusion coefficient. By applying gradients in different directions, a “diffusion tensor” can be mathematically derived using linear algebra, which describes the 3D nature of diffusion. However, diffusion of water molecules *in vivo* can become much more complicated due to complex structural boundaries, such as neurons and axons, leading to non-Gaussian behavior. In order to more accurately model diffusion in the

presence of microstructural boundaries, several methods have been developed which utilize a greater number of b-values. While detrimental to scan time, a greater number of b-values can be acquired by obtaining b-values at greater amplitudes, increasing the number of encoding directions, or a combination of both.

Neurite orientation dispersion and density imaging, or NODDI, is a highly-promising technique designed to probe tissue microstructure more accurately than standard DTI and has been shown to correlate highly with histopathological findings⁵⁸. NODDI attempts to decompose the observed diffusion signal into three different cellular compartments (intra-cellular, extra-cellular, and cerebrospinal fluid [CSF]) based on the anticipated diffusion properties within these compartments. This decomposition is given in Equation 4.

$$S = (1 - V_{iso})(V_{ic}S_{ic} + V_{ec}S_{ec}) + V_{iso}S_{iso}$$

where the term $(1 - V_{iso})$ refers to the normalized non-CSF volume fraction (i.e., restricted diffusion), V_{iso} is the volume fraction of CSF (i.e., unrestricted isotropic diffusion), V_{ic} is the volume fraction of the intra-cellular compartment, V_{ec} is the volume fraction of the extra-cellular compartment, S is the observed diffusion-weighted signal, and S_{ic} , S_{ec} , S_{iso} are the signal components from the intra-cellular, extra-cellular, and isotropic diffusion model, respectively. A visual description of NODDI modelling is shown in Figure 1. The intra-neurite compartment refers to the space bounded by membranes of neurites (specifically, dendrites and axons) with highly-restricted diffusion perpendicular to the length of the

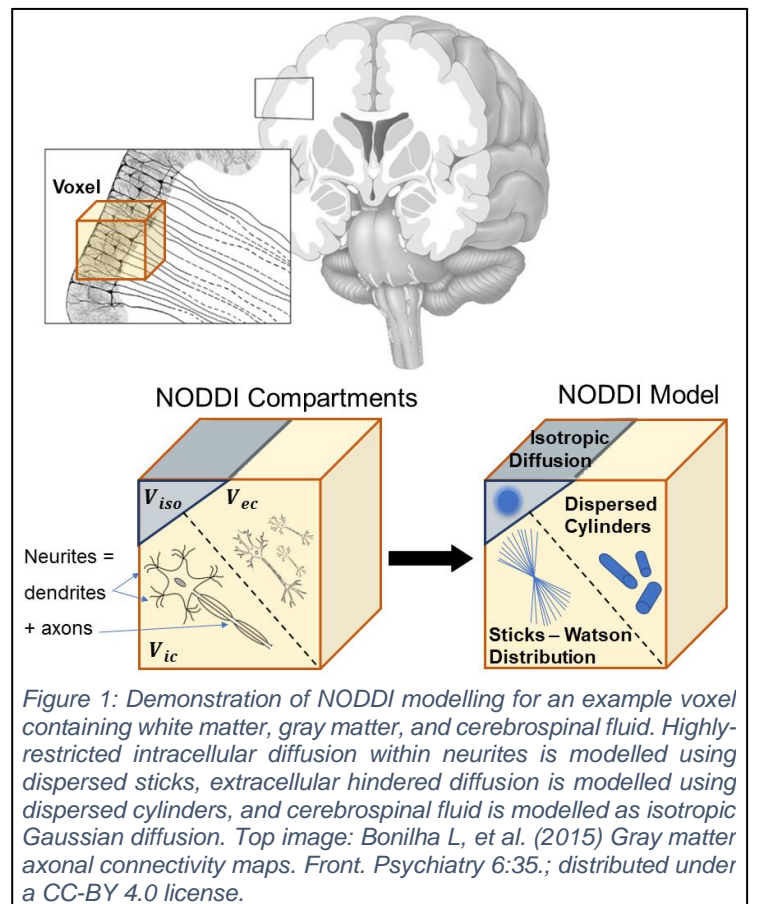


Figure 1: Demonstration of NODDI modelling for an example voxel containing white matter, gray matter, and cerebrospinal fluid. Highly-restricted intracellular diffusion within neurites is modelled using dispersed sticks, extracellular hindered diffusion is modelled using dispersed cylinders, and cerebrospinal fluid is modelled as isotropic Gaussian diffusion. Top image: Bonilha L, et al. (2015) Gray matter axonal connectivity maps. *Front. Psychiatry* 6:35.; distributed under a CC-BY 4.0 license.

axon or dendrite. The intra-neurite compartment is thus best represented by a set of orientation-dispersed “sticks” (using a Watson distribution as the orientation distribution function). The description of this model is out of the scope of this article, but the reader is referred to the articles by Zhang et al.^{42,59} which describe this more thoroughly. The extra-cellular compartment refers to the space *around* the neurites, occupied by glial cells, axons, cell bodies, etc. The diffusion of water is hindered due to these microstructural boundaries, but is not

completely restricted, and is represented by a set of orientation-dispersed cylinders. Again, the reader is referred the articles by Zhang et al^{42,59} for a more comprehensive description of the signal modelling in this compartment. Finally, the CSF compartment is occupied by cerebrospinal fluid and is best modelled by isotropic Gaussian diffusion. Iterative optimization algorithms are then performed to find the signal models that best fit the observed data. Once the signals in each compartment are obtained, the signals are commonly parameterized into neurite density index (NDI), orientation dispersion index (ODI), and isotropic volume fraction (V_{iso}). These parameters can then be mapped for every voxel within a given DTI dataset. The NDI metric reflects the number of neurites for a given signal and will reflect axonal loss in diseases affecting WM. The ODI metric reflects the degree of dispersion, or spreading, of neurites within the intra-cellular compartment which is parametrized by the Dawson's integral from the extra-cellular Watson distribution and bound by the inverse tangent function between values of 0 and 1. In highly-structured WM tracts, as in the corpus callosum, greater ODI values will be observed. Likewise, in crossing fibers and areas of disorganized WM (which may occur due to disease), lower ODI values are expected. In this study, NDI will be the primary metric of interest as this best reflects the degree of axonal degeneration which has been shown to occur in AD.

4D Flow Data Processing

Data for this portion of the study has already been collected from a previous study⁴¹. The use of these measures for this specific study has been discussed and approved by Dr. Leonardo Rivera-Rivera. PWV, PI, and tCBF in the left (LICA) and right internal carotid artery (RICA) have already been computed for each subject. While these data have already been obtained, MRI acquisition parameters, reconstruction methods, and preprocessing steps will be briefly summarized below.

MRI data were acquired using a clinical 3.0T scanner (Discovery MR750, GE Healthcare, Waukesha, WI) with a 32-channel head coil (Nova Medical, Wilmington, MA). 4D flow data were acquired using a radially-undersampled PCVIPR sequence³⁷ using 5-point encoding⁴⁹ ($V_{enc}=80$ cm/s; TR/TE=7.4/2.7 ms; flip angle=8°; voxel resolution=1.7×1.7×1.7 mm³; temporal resolution≈8 ms; reconstructed matrix=320×320×320; number of projections≈11,000). Retrospective cardiac gating was performed using pulse oximeter trigger data.

Velocity-encoded images were retrospectively reconstructed using iterative SENSE⁶⁰ with ESPIRiT⁶¹ sensitivity maps and a local low rank (LLR) constraint, enforcing a local temporal constraint using nuclear norm minimization^{62,63}. Reconstructions were performed with block shifting of a 4×4×4 kernel and an empirically-tuned

regularization parameter ($\lambda=0.01$). Typically, in 4D flow MRI, the temporal resolution is limited by the number of encoding points multiplied by the repetition time (TR). However, in this study, the LLR reconstruction was used to increase the theoretical temporal resolution limit to less than 1 TR (~7.4 ms). Data was reconstructed into 100 cardiac time frames. Several preprocessing algorithms were also used in the reconstruction process including: PILS (Parallel Imaging with Localized Sensitivities) reconstruction to reduce the spread of undersampling artifacts, correction of Maxwell term phase offsets⁶⁴, 4D Laplacian unwrapping to automatically correct velocity aliasing⁶⁵, and 3rd-order polynomial background phase correction for eddy current phase offsets⁶⁴.

An automated cranial 4D flow processing tool was used to calculate PI and tCBF, in which cut-planes were automatically generated along vessel centerlines for automatic data extraction⁶⁶. PI values and volumetric flow rates (blood flow) were computed from within cut-planes placed in the left and right cervical internal carotid arteries (ICA). A final PI value was obtained by averaging PI values between the left and right cervical ICAs. Total cerebral blood flow was computed by summing the volumetric flow rates in the left cervical ICA, right cervical ICA, and basilar artery. For PWV calculation, the temporal shift in flow waveforms between cut-planes placed in the left cervical ICA and left petrous ICA was estimated using time-to-foot methods from the resultant flow curves⁶⁷. Distance was calculated between measurement points from the automatically-generated vessel centerline using the cranial 4D flow processing tool. Finally, to compute PWV, the calculated distance between measurement points was divided by the calculated time shift in the flow waveforms. The same process was repeated in the right ICA and PWV values in the left and right ICAs were averaged.

NODDI Data Processing

MRI data were acquired using a clinical 3.0T scanner (Discovery MR750, GE Healthcare, Waukesha, WI) with a 32-channel head coil (Nova Medical, Wilmington, MA). T1-weighted structural images were acquired using a 3D inversion recovery prepared fast spoiled gradient-recalled echo (BRAVO) sequence (TI=450 ms; TR/TE=8.2/3.2 ms; flip angle=12°; 1×1×1 mm³ voxel resolution; 256×256×[156-192] acquisition matrix). A multi-shell spin-echo echo-planar imaging pulse sequence was used to acquire 69 total diffusion-weighted images spread across 4 q-space shells (6×b=0 s/mm², 9×b=500 s/mm², 18×b=800 s/mm², and 36×b=2000 s/mm²; TR/TE=8575/76.8 ms; 2×2×2 mm³ isotropic resolution; 128×128×[74-92] acquisition matrix).

A desktop computer system (Dell Precision 5820 Tower, Intel Xeon W-2123 3.60 GHz CPU, 32 gigabytes RAM) running Windows 10 was used to power a virtual environment containing FMRIB software library (FSL;

<https://fsl.fmrib.ox.ac.uk/fsl>⁶⁸ and MRtrix3 (<https://mrtrix.org>)⁶⁹. Twenty-two gigabytes of RAM were allocated to the virtual machine and 4 cores were dedicated for processing. Raw diffusion-weighted images (DWIs) were denoised using *dwidenoise*⁷⁰ and corrected for Gibb's ringing artifact using *mrdegibbs*⁷¹. Skull-stripping and brain matter segmentation was accomplished using *BET*⁷². Finally, eddy current correction was performed using *eddy*⁷³. Image quality and subject motion was quantitatively assessed for each subject using the summarized quality control outputs from the *eddy_quad* tool⁷⁴. Slices with significant signal loss caused by subject motion were automatically detected and replaced using predictions made by a Gaussian process⁷⁵.

DTIs were estimated from the pre-processed data using *dtifit*⁷⁶. The NODDI MATLAB Toolbox (<http://mig.cs.ucl.ac.uk>)⁴² was used to model NODDI parameter maps (NDI, ODI, and V_{iso}) from the DTIs in MATLAB R2020b (The Mathworks Inc., Natick, MA). Additionally, the Parallel Computing Toolbox in MATLAB was employed to expedite NODDI processing. Tract-based spatial statistics (TBSS) was then used to visualize and assess areas of significance in the NDI maps⁷⁷. In order to perform TBSS, processing was first performed on the FA images. Each FA image was morphologically eroded and end slices were zeroed to remove likely outliers from the diffusion tensor fitting. Nonlinear registration with intermediate degrees of freedom was performed using *FNIRT*⁷⁸ to co-register all FA images to 1 mm³ FMRIB58 FA standard space. Next, the mean FA image was created and thinned to create a mean FA skeleton representing the tract centers common to all subjects. The NDI data was then projected onto this skeleton and voxel-wise cross-subject statistics was performed and visualized in *FSLeyes*. Localized clusters of significance were identified and recorded.

Subjects

A total of 20 AD and 41 age-matched cognitively normal (CN) control subjects have been identified from the Wisconsin Alzheimer's Disease Research Center (ADRC) and Wisconsin Registry for Alzheimer's Prevention (WRAP) protocols. The University of Wisconsin Institutional Review Board approved all study procedures and all subjects provided signed written informed consent before participation in MRI scanning. Datasets from all subjects were transferred from the ADRC server database to the University of Wisconsin Medical Physics servers after submission of a UP request, required for retrospective data analysis on ADRC and WRAP participants. All data transfer and storage was Health Insurance Portability and Accountability Act (HIPAA) compliant. Precalculated PWV, PI, and tCBF metrics were matched to each patient. Demographic data for both cohorts

were also obtained and are shown in Table 1. Note propensity matching⁷⁹ was not performed prior to data analysis.

Table 1. Subject demographics.

	Total (N = 61)	CN (N=41)	AD (N = 20)	p-value
Age (years)	73 ± 8	74 ± 7	73 ± 9	0.96 ^a
Female (n, %)	36, 59.0	23, 56.1	13, 65.0	0.58 ^b
Parental history of dementia (n, %)	8, 13.1	1, 2.44	7, 35.0	0.001^b
APOE ε4 carrier (n, %)*	7, 11.5	1, 2.44	6, 30.0	2.51e-04^b
SBP (mmHg)	132 ± 21	132 ± 22	131 ± 19	0.78 ^c
DBP (mmHg)	77 ± 8	78 ± 9	75 ± 6	0.23 ^c
HR (bpm)	61 ± 10	62 ± 9	60 ± 11	0.55 ^c

CN=cognitively normal; AD=Alzheimer's disease; APOE=apolipoprotein E; SBP=systolic blood pressure; DBP=diastolic blood pressure; HR=heart rate
*Eight AD subjects were not genotyped; carrier is defined as presence of at least one allele
^aTwo sample t-test, assuming unequal variance (variance assess with F-test); ^bFisher's exact test (categorical data); ^cTwo sample t-test, assuming equal variance (variance assess with F-test); **Bold** indicates statistical significance (p<0.05)

Statistical Analysis

Two-sample t-tests were performed in MATLAB R2020b to assess group differences in PI, PWV, and tCBF measurements. TBSS⁷⁷ and *Feat*⁸⁰ in FSL were then used to create design matrices, create contrasts, and to visualize whole-brain WM differences between AD and CN groups. Design matrices included age and sex for adjustment of these covariates during statistical analysis. Design contrasts assessed two-way group differences in NDI, positive and negative correlations between NDI and each cerebrovascular metrics (PWV, PI, and tCBF) for both CN and AD groups, and differences in correlation between groups (i.e. comparison of adjusted regression coefficients). Non-parametric permutation tests (N=5,000) with threshold-free cluster enhancement was performed using *randomise*⁸¹.

Post hoc region of interest (ROI)-based analysis was performed primarily in MATLAB 2020b to test group differences in NDI and correlations between NDI and cerebrovascular metrics. Significant clusters on the skeletonized statistical maps were visually identified in *FSLeys* after performing TBSS and WM regions associated with significant regions were identified using

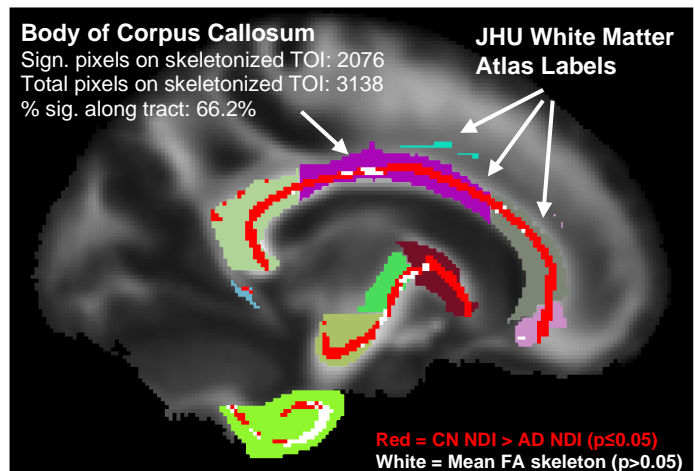


Figure 2: Process for quantifying significance over tracts of interest (TOI). First, the mean FA skeleton is multiplied by the JHU white matter atlas, giving a skeletonized atlas. Then, the percentage of sign. (significant) pixels for each tract (for a given hypothesis test) is computed. An example is shown for calculating this percentage in the body of the corpus callosum.

the JHU ICBM labels 1mm Atlas (<https://identifiers.org/neurovault.image:1401>). To quantify the amount of statistically significant voxels that were observed within each ROI, the WM atlas was skeletonized (through pointwise multiplication with the mean FA skeleton) and the percentage of significant voxels along each tract of interest (TOI) was computed (Figure 2). The non-skeletonized atlas was then used to extract mean NDI values for each patient within the identified ROIs. Analysis of covariance (ANCOVA) tests were performed to assess group differences in NDI measures after adjusting for age, sex, and correcting for multiple comparisons using a Bonferroni correction. Fixed-effect linear regression models were used to evaluate associations in mean NDI for each ROI and each cerebrovascular metric (PWV, PI, and tCBF) between both groups after adjusting for age, sex, interaction terms, and correcting for multiple comparisons.

Results:

4D Flow and Demographics Analysis

4D flow data was successfully obtained and matched to the diffusion tensor imaging (DTI) datasets that were obtained for the 41 CN and 20 AD subjects. Statistical analysis of demographic information showed no significant differences in age, sex, blood pressure, and heart rate between the two groups, but did show significant differences in parental history of dementia and APOE status (Table 1). Analysis of the 4D flow data revealed significant differences in pulse wave velocity (PWV) between AD and CN groups. However, PI and tCBF metrics were not significantly different. These results are in agreement with published work from Rivera-Rivera et al⁴¹. A summarized analysis is provided in Table 2.

Table 2. Summary results from 4D flow cerebrovascular analysis.

	CN (N=41)	AD (N = 20)	p-value	Effect Size (Cohen's d)
Average ^a PWV (m/s)	17.5 ± 9.17	27.9 ± 9.77	1.4e-04*	0.78
Average ^a PI (unitless)	1.25 ± 0.23	1.29 ± 0.30	0.56	0.11
tCBF ^b (mL/s)	3.46 ± 0.66	3.19 ± 0.88	0.17	-0.26

Abbreviations: CN=cognitively normal; AD=Alzheimer's disease; PWV=pulse wave velocity;
PI=pulsatility index; tCBF=total cerebral blood flow

^aAveraged between left and right internal carotid arteries.

^bSum of flow from left internal carotid, right internal carotid, and basilar arteries.

*p-values<0.05

NODDI Processing

DTI data were successfully corrected in FSL. A detailed analysis of motion (produced by the *eddy_squad* function in FSL) is provided in Appendix Figure 1A. DTI parameters, including fraction anisotropy (FA), were approximated in FSL. Non-linear image registration of the FA images to the FMRIB FSL FA template showed

excellent co-registration between images. This was performed automatically using the TBSS registration script, however, doing this led to some brain regions being erroneously masked primarily in the posterior aspect of the brain. Despite this, most brain regions were included after registration. Processing of NODDI images in MATLAB 2020b took approximately 5 hours per case, creating volumetric NDI, ODI, and V_{iso} maps for each subject. Note that only NDI maps were retained for analysis in this study. FA and NDI maps for a single CN and AD subject are shown in Figure 3.

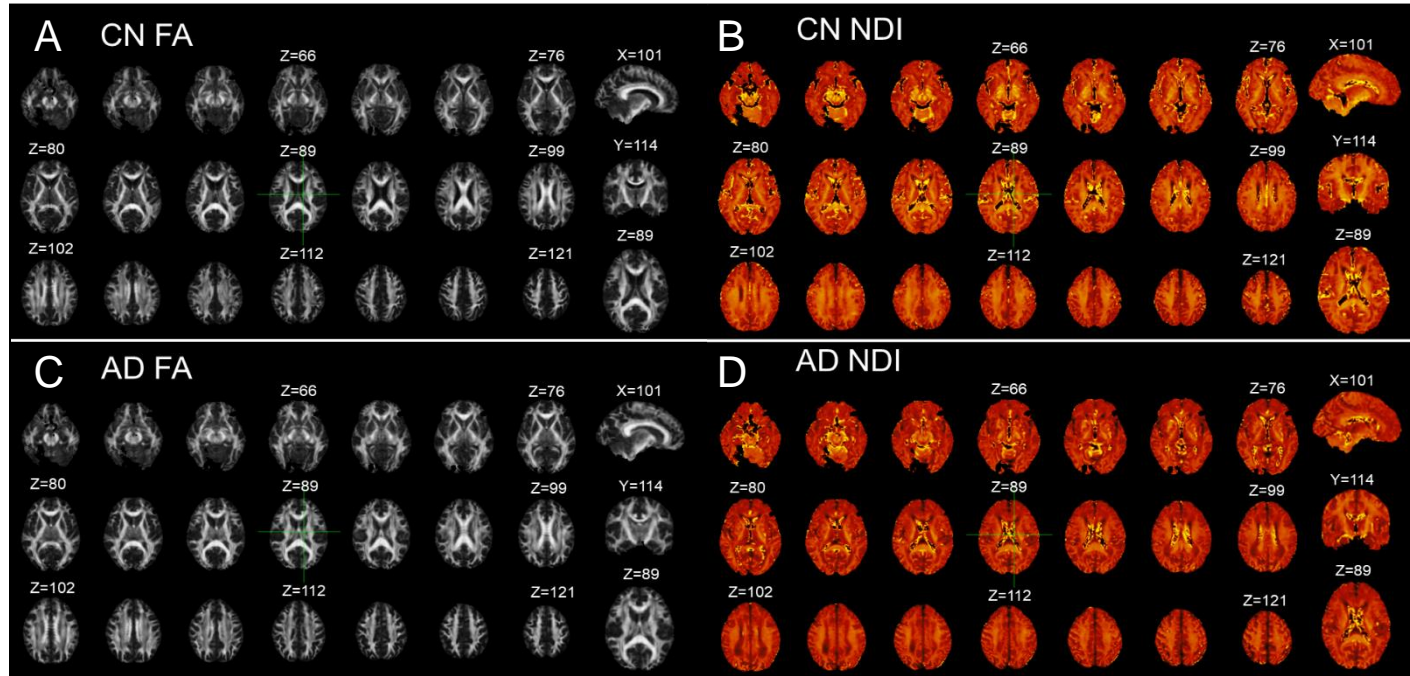


Figure 3: Fractional anisotropy (FA) images for a cognitively normal (CN) subject (A) and Alzheimer's disease (AD) subject (C). Neurite density index (NDI) maps shown for the same CN subject (B) and AD subject (D).

NDI Analysis

Tract-based spatial statistics (TBSS) revealed a large number of voxel-wise differences when testing if AD subjects have greater NDI values compared to CN subjects, as shown in Figure 4.

Significant tracts were identified and are listed in Table 3. The statistical maps testing if NDI values were greater in AD subjects compared to CN subjects did not show any significant voxels.

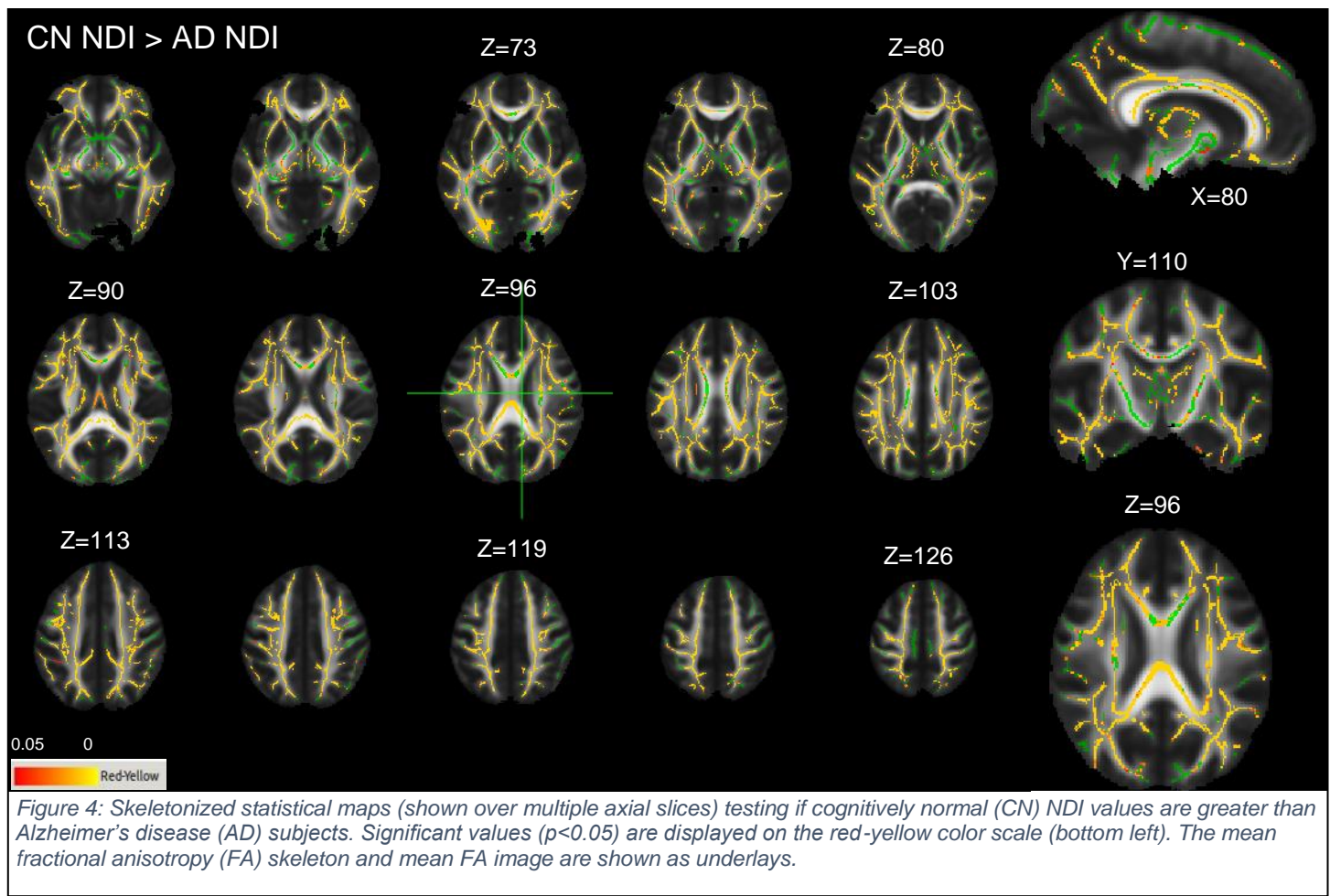


Table 3. NDI statistical analysis between AD and CN cohorts.

	CN NDI > AD NDI?				
White Matter Regions Identified from TBSS (JHU Label #)	% sig. voxels ^a	AD Mean NDI	CN Mean NDI	p-value	Confidence Intervals
Genu of Corpus Callosum (3) †	77.3	0.5264	0.5083	0.1329	-0.006, 0.042
Body of Corpus Callosum (4)	66.2	0.5946	0.5738	0.0137*	0.004, 0.037
Splenium of Corpus Callosum (5)	93.3	0.6358	0.5986	5.2e-05**	0.020, 0.054
Anterior corona radiata R (23)	88.9	0.4726	0.4394	0.0138*	0.007, 0.059
Anterior corona radiata L (24)	99.1	0.4735	0.4299	0.0019**	0.017, 0.070
Superior corona radiata R (25)	88.8	0.5896	0.5573	0.0113*	0.008, 0.057
Superior corona radiata L (26)	95.9	0.5825	0.5411	0.0024*	0.015, 0.068
Posterior corona radiata R (27)	88.4	0.5120	0.4748	0.0153*	0.007, 0.067
Posterior corona radiata L (28)	93.6	0.5048	0.4682	0.0104*	0.009, 0.064
Posterior thalamic radiation R (29)	86.3	0.5160	0.4762	3.9e-04**	0.019, 0.061
Posterior thalamic radiation L (30)	84.9	0.4872	0.4394	3.3e-04**	0.023, 0.073
Sagittal stratum R (31) †	93.6	0.5105	0.4942	0.0558	-0.004, 0.033
Sagittal stratum L (32) †	82.1	0.4874	0.4680	0.0541	-0.004, 0.039
External capsule R (33)	73.1	0.5061	0.4868	0.0075*	0.005, 0.033
External capsule L (34)	82.5	0.5089	0.4840	2.9e-04**	0.012, 0.038
Cingulate gyrus R (35)	98.8	0.5363	0.5114	7.8e-05**	0.013, 0.037
Cingulate gyrus L (36)	96.8	0.5420	0.5120	8.4e-06**	0.018, 0.042
Cingulum (hippocampus) R (37)	91.8	0.4970	0.4647	2.8e-04**	0.016, 0.049
Cingulum (hippocampus) L (38)	93.8	0.4945	0.4711	3.5e-04**	0.011, 0.036
Superior longitudinal fasciculus R (41)	94.1	0.5920	0.5592	0.0069*	0.009, 0.056
Superior longitudinal fasciculus L (42)	98.1	0.5944	0.5534	7.8e-04**	0.018, 0.064
Superior fronto-occipital fasciculus R (43)	48.7	0.5553	0.5187	0.0317*	0.003, 0.070
Superior fronto-occipital fasciculus L (44)	98.9	0.5397	0.4795	0.0026*	0.022, 0.099
Uncinate fasciculus R (45)	100	0.4838	0.4528	2.9e-05**	0.017, 0.045
Uncinate fasciculus L (46)	100	0.4833	0.4514	1.6e-05**	0.018, 0.046

Abbreviations: JHU=Johns Hopkins University; ROI=region of interest; Sig.=significant; R=right; L=left

^aPercentage of significant voxels (obtained from TBSS) along skeletonized tract label (see Figure 2).

†Non-significant ROI analysis. **Bold** indicates statistical significance.

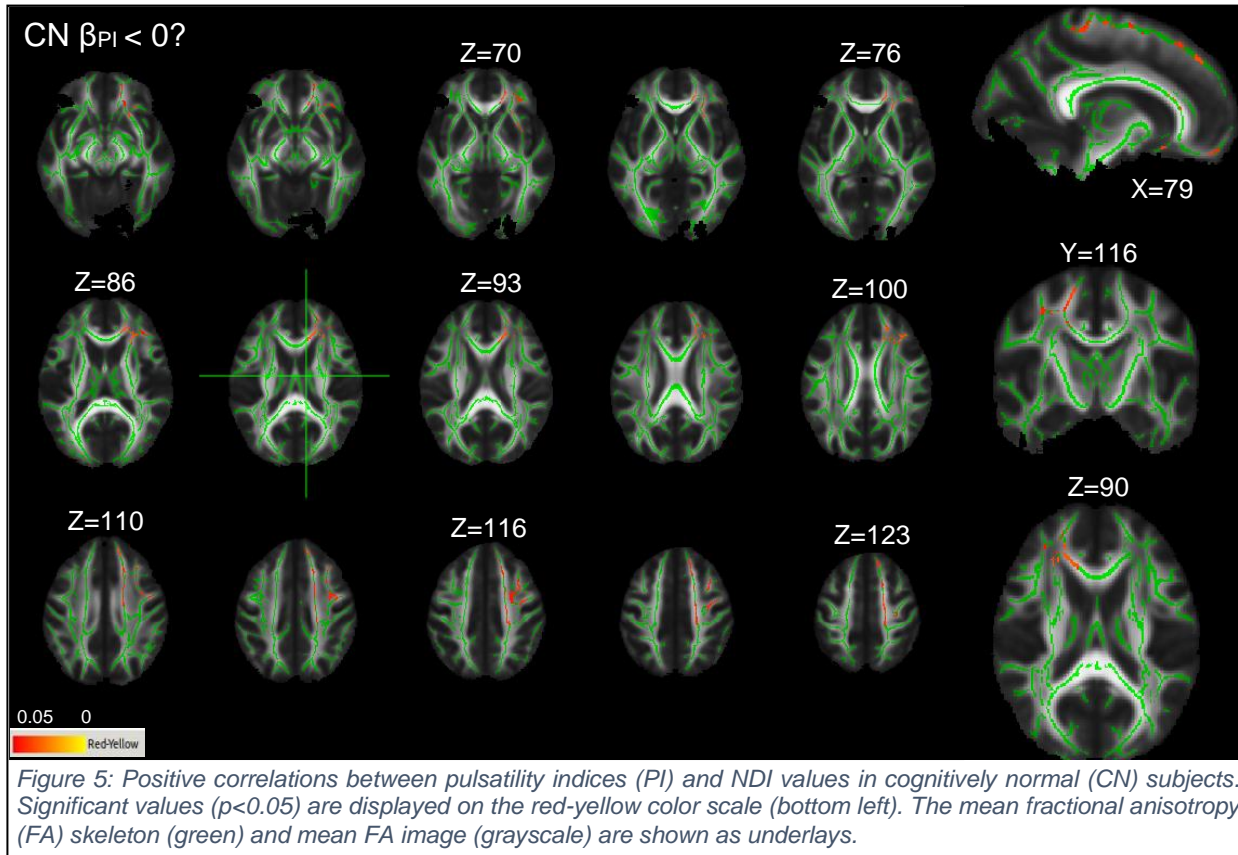
*p-values <0.05; **p-value<0.002 (Bonferroni correction for 25 ROIs).

Region of interest (ROI)-based analysis using the Johns Hopkins University (JHU) white matter 1mm atlas was successfully performed on the tracts identified from TBSS. Twenty-five tracts in total were visually identified from the TBSS statistical maps. Analysis of covariance (ANCOVA) revealed significant differences in a number white matter (WM) regions, including the splenium of the corpus callosum, left anterior and superior corona radiata, right and left posterior thalamic radiation, left external capsule, right and left cingulate gyrus, right and left cingulum, left superior longitudinal fasciculus, and the right and left uncinate fasciculus. Note, however, that there were a number of other tracts that did not survive Bonferroni correction but had a p-value of less than 0.05.

Additionally, tracts that were visually identified from TBSS demonstrated a high number of significant pixels along the skeletonized WM atlas.

Correlations between NDI and Cerebrovascular Metrics

TBSS did not reveal any significant correlations (positive or negative) between PWV and NDI for either the AD or CN groups as visualized by the statistical maps. PI was negatively correlated with NDI for the CN group, but the regions of significance were relatively sparse (Figure 5). This correlation was not observed for the AD group.



Regions that were identified on the statistical map testing for negative PI correlations in the CN group did not demonstrate significant differences after performing ROI analysis (Table 4). Additionally, the 3 ROIs that were identified from the PI correlation analysis did not have a large percentage of significant voxels along the skeletonized WM atlas.

Table 4. PI and NDI correlation analysis in cognitively normal subjects.

	CN $\beta_{PI} < 0?$			
White Matter Regions Identified from TBSS (JHU Label #)	% sig. voxels ^a	β_{PI}	R ²	p
Genu of corpus callosum (3)	11.3	-0.025	0.041	0.434
Anterior corona radiata R (23)	51.1	-0.081	0.292	0.035*
Posterior corona radiata R (27)	11.2	-0.051	0.106	0.222

Abbreviations: JHU=Johns Hopkins University; Sig.=significant; R=right; L=left
^aPercentage of significant voxels (obtained from TBSS) along skeletonized tract label (see Figure 2).
p*-values <0.05; *p*-values > 0.017 (Bonferroni correction for 3 ROIs).

Lastly, TBSS demonstrated significant voxels in many regions in which tCBF was positively correlated with NDI in CN subjects (Figure 6). Additionally, TBSS statistical maps assessing whether tCBF correlations (i.e., beta coefficients or slopes) were significantly different between groups showed significance in similar regions (Figure 7). ROI-based fixed-effect linear regression only showed significance in the right superior longitudinal fasciculus after Bonferroni correction (Table 5). However, it is noted that several other regions, specifically the corpus callosum and corona radiata, had *p*-values of less than 0.05. It was also observed that the lowest *p*-values tended to be associated with the largest number of significant voxels (from TBSS) along tracts of interest. ROI-based assessment of differences between tCBF-NDI correlations also showed significant differences in the right

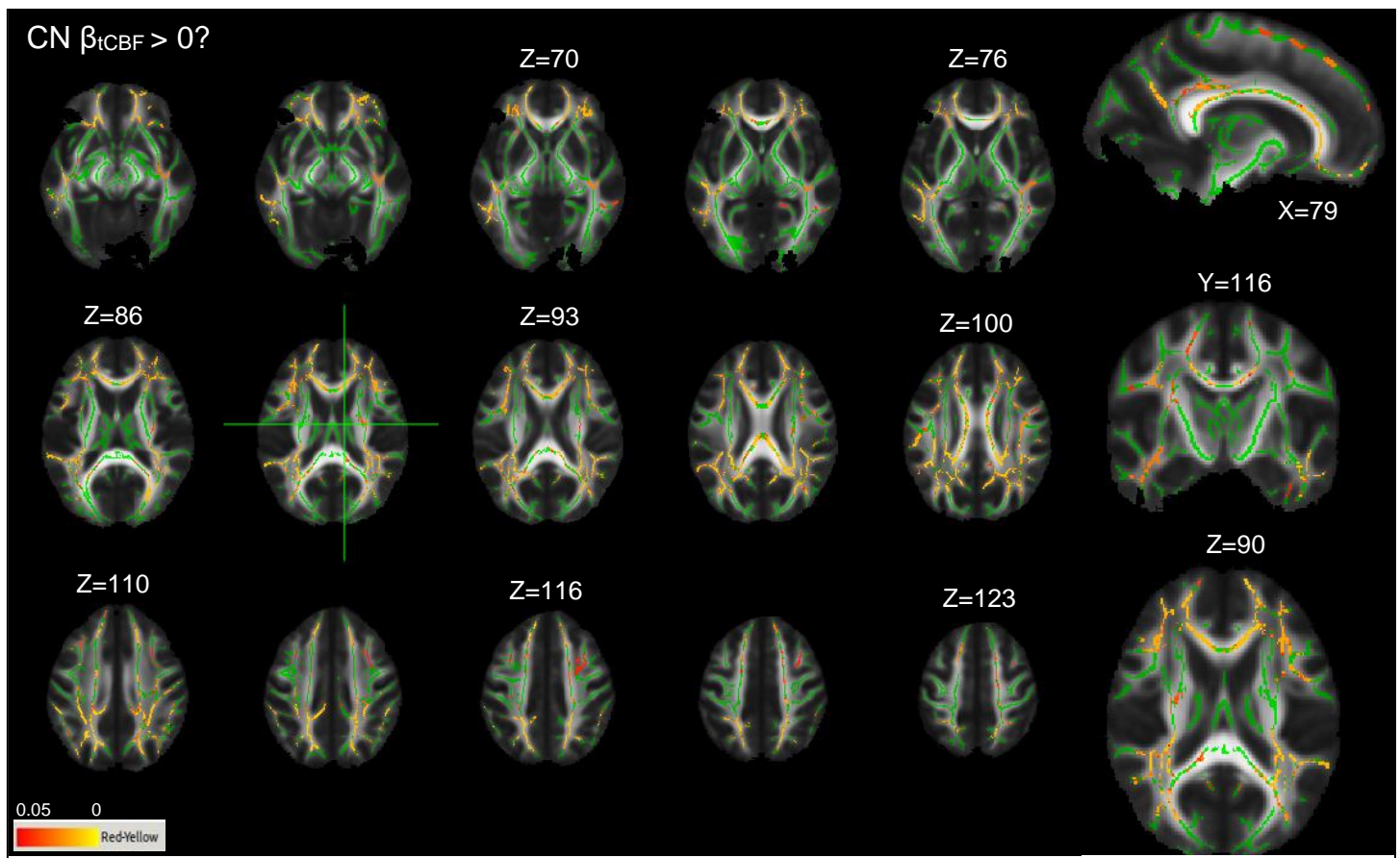


Figure 6: Positive correlation between total cerebral blood flow (tCBF) and NDI in cognitively normal (CN) subjects.

and left superior longitudinal fasciculus (Table 6). Adjusted tCBF-NDI regression plots for ROIs in the superior longitudinal fasciculus and posterior corona radiata are provided in Figures 8-9

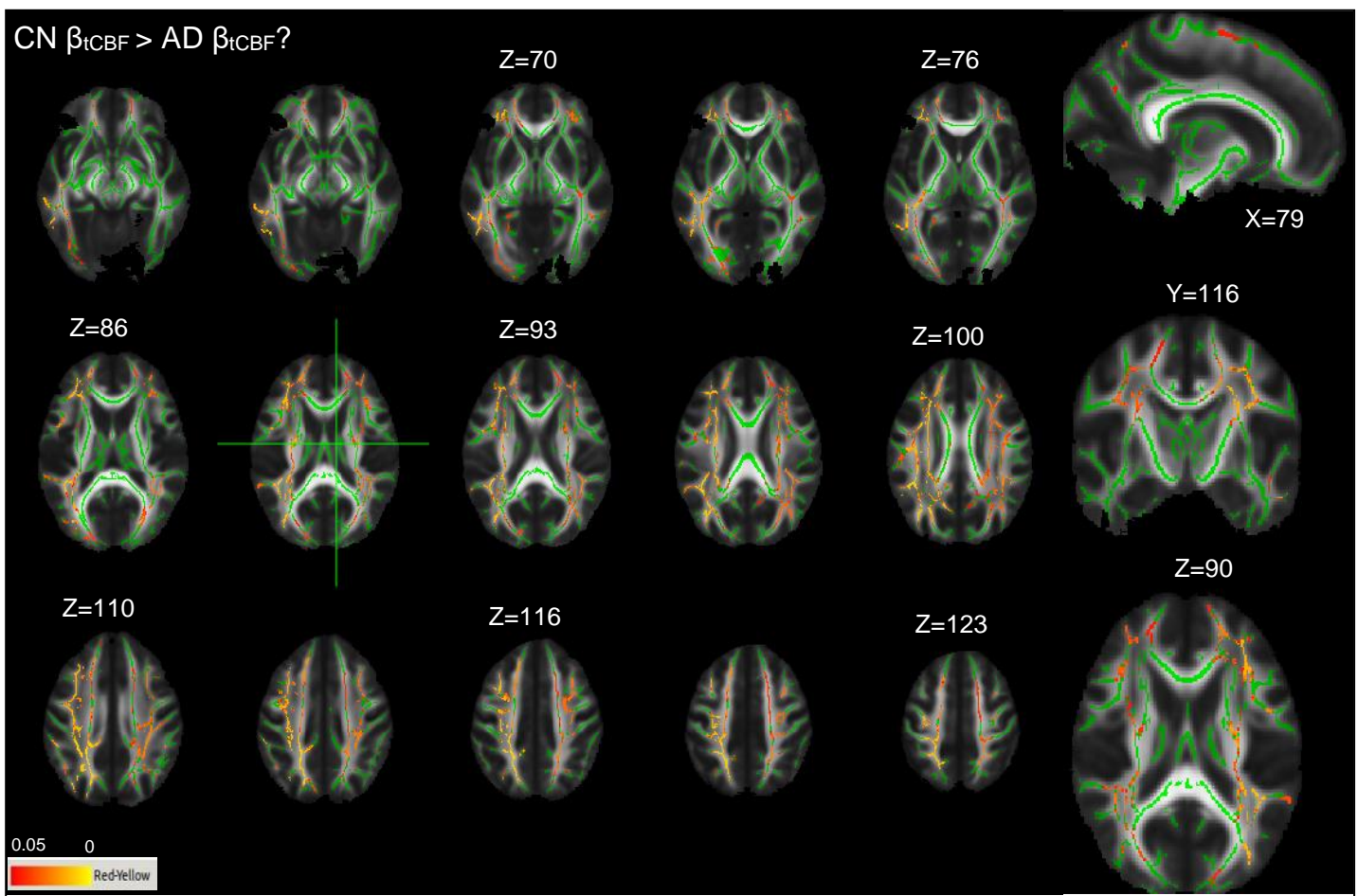


Figure 7: Differences in the correlation between total cerebral blood flow (tCBF) and NDI (slope coefficients) between cognitively normal (CN) subjects and Alzheimer's disease (AD) subjects.

Table 5. tCBF and NDI correlation analysis in cognitively normal subjects.

	CN $\beta_{tCBF} > 0?$				CN $\beta_{tCBF} > AD \beta_{tCBF}?$
White Matter Regions Identified from TBSS (JHU Label #)	% sig. voxels ^a	β_{tCBF}	R ²	p-value	p-value
Genu of corpus callosum (3)	6.10	0.025	0.129	0.019*	0.760
Body of corpus callosum (4)	19.4	0.025	0.247	4e-04*	0.067
Splenium of corpus callosum (5)	12.0	0.019	0.176	0.013*	0.248
Anterior corona radiata R (23)	6.55	0.026	0.283	0.045*	0.113
Anterior corona radiata L (24)	38.6	0.027	0.212	0.034*	0.037*
Superior corona radiata R (25)	80.8	0.019	0.237	0.075	0.004*
Superior corona radiata L (26)	75.8	0.015	0.174	0.203	0.006*
Posterior corona radiata R (27)	75.8	0.036	0.245	0.007*	0.007*
Posterior corona radiata L (28)	84.8	0.035	0.216	0.008*	0.006*
Posterior thalamic radiation R (29)	31.5	0.020	0.206	0.049*	0.016*
Posterior thalamic radiation L (30)	57.0	0.021	0.169	0.078	0.009*
Superior long. fasciculus R (41)	76.7	0.028	0.349	0.001**	6e-05**
Superior long. fasciculus L (42)	89.3	0.023	0.221	0.012*	5e-04**

Abbreviations: JHU=Johns Hopkins University; Sig.=significant; R=right; L=left

^aPercentage of significant voxels (obtained from TBSS) along skeletonized tract label (see Figure 2).

*p-values <0.05; **p-value<0.004 (Bonferroni correction for 13 ROIs).

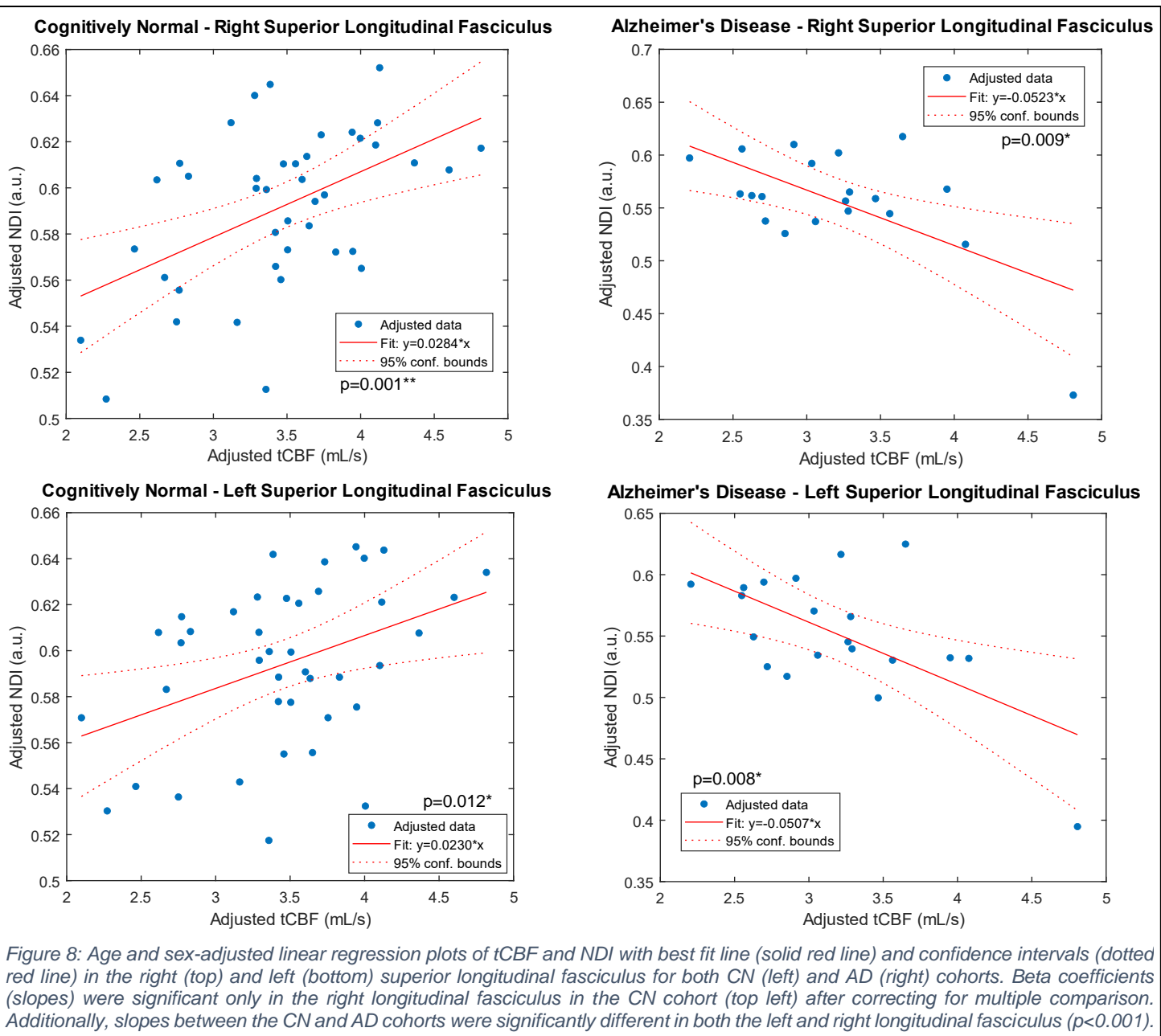


Figure 8: Age and sex-adjusted linear regression plots of tCBF and NDI with best fit line (solid red line) and confidence intervals (dotted red line) in the right (top) and left (bottom) superior longitudinal fasciculus for both CN (left) and AD (right) cohorts. Beta coefficients (slopes) were significant only in the right longitudinal fasciculus in the CN cohort (top left) after correcting for multiple comparison. Additionally, slopes between the CN and AD cohorts were significantly different in both the left and right longitudinal fasciculus ($p<0.001$).

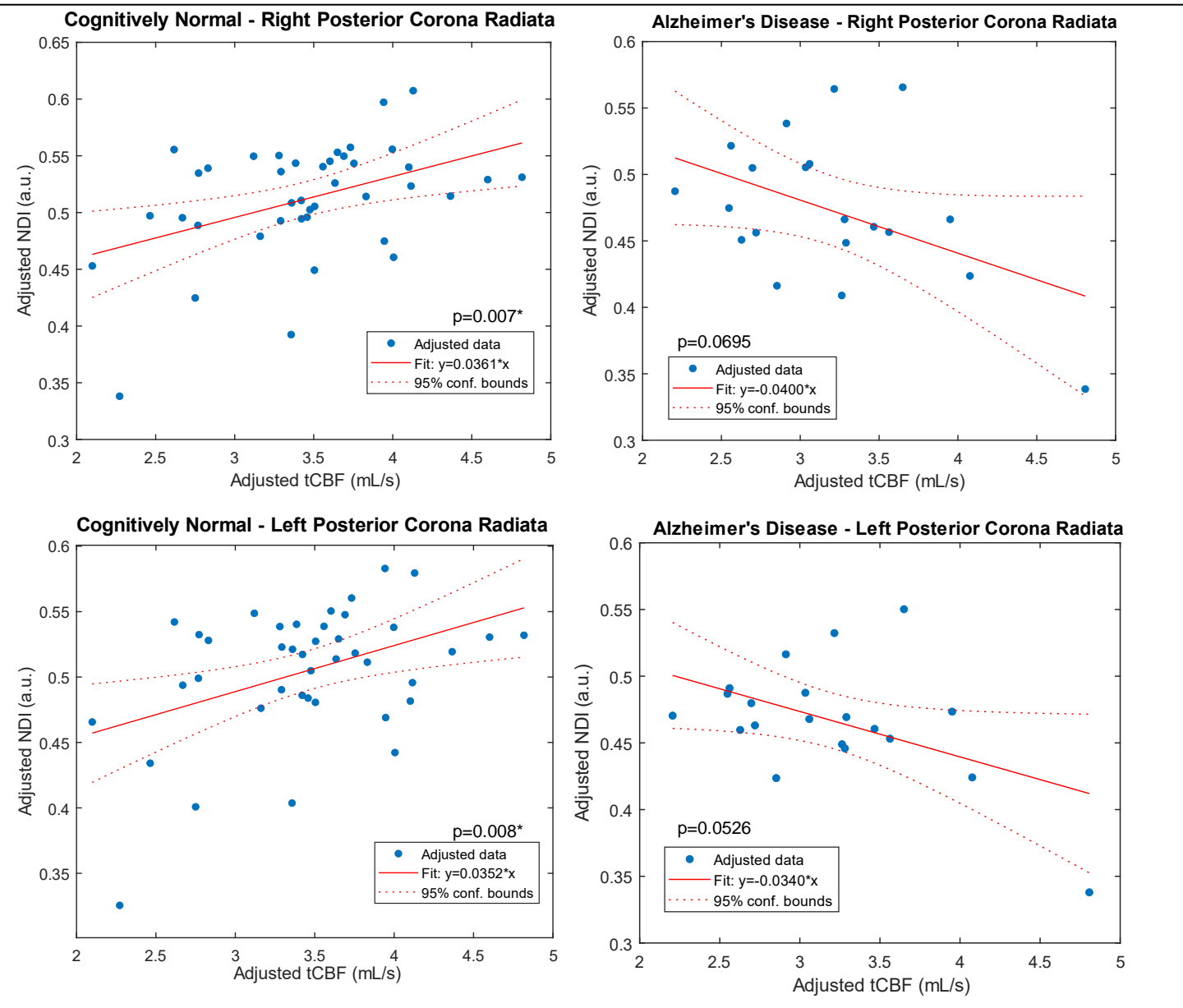


Figure 9: Age and sex-adjusted linear regression plots of tCBF and NDI with best fit line (solid red line) and confidence intervals (dotted red line) in the right (top) and left (bottom) posterior corona radiata for both CN (left) and AD (right) cohorts. Beta coefficients (slopes) were not significant after correcting for multiple comparison. However, positive trend was observed in the CN cohort and a negative trend was observed in the AD cohort, similar to the results in the superior longitudinal fasciculus.

Discussion:

In this study, 4D flow MRI and neurite orientation dispersion and density imaging (NODDI) were used to simultaneously assess cerebrovascular hemodynamics and white matter axonal density in 41 cognitively normal (CN) and 20 Alzheimer's disease (AD) subjects. Specifically, pulse wave velocity (PWV), pulsatility index (PI), and total cerebral blood flow (tCBF) values were used as surrogate metrics for global cerebrovascular health. It has been reported in several studies that PWV and PI are increased and tCBF is decreased in individuals with AD^{25,28,38,39,41}. Likewise, AD-related white matter (WM) microstructure degeneration has also been observed in

various WM tracts using NODDI^{13,15,16}. Our results are consistent with the findings from these studies. However, increased PI and decreased tCBF in AD subjects relative to CN subjects was not observed. This may be due to the modest sample sizes in this study. Secondarily, image quality could not be assessed as the raw 4D flow data was not provided, only the PWV, PI, and tCBF values for each subject that had been computed prior to this study (provided by Rivera-Rivera LA with results reported in a previous study⁴¹). Velocity noise can greatly affect PI measurements because the maximum blood velocity value (over time) is used as the numerator in this calculation, which can result in erroneous increases in PI.

TBSS analysis of NDI showed a large number of areas on the WM skeleton that were significantly differently between groups. ROI-based analysis on these tracts demonstrated a decrease in neurite density index (NDI) for the AD cohort in the corpus callosum, anterior and superior corona radiata, posterior thalamic radiation, left external capsule, cingulate gyrus, cingulum, superior longitudinal fasciculus, and uncinate fasciculi. Decreased NDI metrics are likely reflective of white matter degeneration and axonal loss in the AD cohort. In most cases, significance was bilateral and results were in good visual agreement with TBSS results from other studies, namely the study by Fu et al¹³ (numerical results for AD vs. CN were not provided). Other studies, such as the study by Slattery et al, did not perform tract-specific analysis but instead performed analysis on WM quadrants¹⁵. Nonetheless, the study by Slattery et al. demonstrated widespread changes in NDI which is consistent with the findings from this study. Finally, the study published by Wen et al. did not compare AD vs. CN, but rather compared mild cognitive impairment (MCI) and subjective cognitive decline (SCD) individuals to CN individuals¹⁶. The study by Wen et al. (using tractography-based ROI analyses) did not find differences in NDI between SCD, MCI, or CN groups.

While PWV was significantly different between groups, TBSS did not reveal any correlations (positive or negative) between PWV and NDI for either group. Some negative correlations between PI and NDI were observed on the TBSS statistical maps, however, significant clusters were sparse and were not significantly different upon performing ROI analysis. Surprisingly, there were many areas in which tCBF was positively correlated with NDI in the CN group. Furthermore, similar areas also showed differences in correlation between CN and AD groups. While ROI analysis only showed significant correlations in the CN group (and correlation differences between CN and AD groups) in the superior longitudinal fasciculus, other areas showed trends of positive correlation. These findings may be clinically relevant as it may reflect early stages of vascular dementia

that is occurring in CN subjects, which is the second most common cause of dementia after AD and may be underdiagnosed in many individuals⁸². It is possible that decreased cerebral blood flow, caused by global cardiovascular disease, such as increased blood pressure, atherosclerosis, heart disease, etc., is leading to changes in WM degeneration. On the other hand, it may be possible that microscopic neurovascular insults are leading to changes in microcirculation, which is then leading to observed changes in cerebral blood flow. However, given data from the current study, it is difficult to address this potential causative association. It is hypothesized that the lack of significant correlations between CV measures and NDI in the AD cohort is the result of WM damage that has already occurred, and thus there is not a strong relationship between these metrics. Furthermore, while not statistically significant, there were some trends of negative correlation between tCBF and NDI in the AD group, particularly in the superior longitudinal fasciculus. An explanation for this negative relationship is not readily apparent.

Limitations:

There were several major limitations to this study. First, sample sizes for the AD group were relatively small (N=20), reducing statistical power and increasing error in statistical analysis. Second, white matter hyperintensities were not accounted for prior to NODDI processing. It has been shown that NODDI estimates may deviate in white matter hyperintensities, leading to distortions in parameter estimation⁸³. Third, data fidelity of the 4D flow images could not be assessed because the raw image and gating files were not provided. Future studies will analyze such CV measures independently, instead of relying on already processed data. Lastly, utilizing global CV metrics obtained from the major cerebral arteries may lead to decreased specificity. For instance, obtaining regional measures of CV flow and pulsatility in smaller vessels (using 4D flow and/or arterial spin labelling techniques) and correlating these measures spatially with NDI measurements may provide for more specific information related to the effects of CV disease.

Other limitations of the study include performing atlas-based ROI analyses. It has been shown that combining automated tractography-based and ROI-based may lead to more optimal results^{84,85}. Additionally, analyses of other NODDI metrics, including ODI and V_{iso} , could have been performed. Such maps were chosen to not be analyzed in order to increase the focus and brevity of the current paper. However, studies by Slattery et al., Wen et al., and Fu et al. suggest that these metrics are also altered in AD and MCI subjects^{13,15,16}. These results may offer more insights into the observed microstructural changes in the current study.

Future directions:

Future studies aim to evaluate AD in the preclinical stage, namely in the MCI stage. Both 4D flow and multi-shell DTI for such patients exist at the Wisconsin ADRC and can be readily obtained for analysis upon appropriate request. The acquisition of longitudinal datasets (which also have been obtained at the Wisconsin ADRC) may allow for the assessment of causal inferences of WM degeneration and cerebral blood flow alterations in CN individuals. Cognitive batteries (such as Mini-Mental State Exam or Montreal Cognitive Assessment) are also performed in ADRC subjects and could be used as additional covariates. Future studies may also look to verify AD and MCI status by utilizing amyloid/tau PET imaging and cerebrospinal fluid biomarkers. Lastly, it has been shown by Wen et al. and Fu et al. that there is a posterior-anterior gradient in NODDI metrics in WM across the spectrum of AD, similar to the spread of tau deposition which is consistent with Braak staging^{86,87}. This suggests that NODDI measures may correlate with tau; one study has shown that there are significant correlations between NDI and tau protein deposition in mouse models⁸⁸. Assessing the spatial extent of tau deposition from PET scans simultaneously with NODDI across the AD spectrum may also provide interesting results.

Conclusion:

This study demonstrated significant alterations in WM microstructure, specifically decreases in axonal density, in AD patients in various WM tracts. These findings further support findings from other studies assessing WM microstructural changes in AD subjects. Additionally, decreased cerebral blood flow in the major cerebral arteries were significantly correlated with decreased NDI values, primarily in the superior longitudinal fasciculus. However, similar correlational trends existed in other white matter structures. Such findings may reflect subtle vascular changes occurring in cognitively normal subjects that may reflect prodromal vascular dementia in this older cohort. No associations between global cerebrovascular health measures and NDI were found in the AD group. Increased sample sizes, assessment in MCI cohorts, and longitudinal assessments are highly-warranted to verify these findings and strengthen causal inferences.

Bibliography and References Cited:

- 1 Nasrabady, S. E., Rizvi, B., Goldman, J. E. & Brickman, A. M. White matter changes in Alzheimer's disease: a focus on myelin and oligodendrocytes. *Acta Neuropathol Commun* **6**, 22-22, doi:10.1186/s40478-018-0515-3 (2018).
- 2 Krajcovicova, L., Klobusikova, P. & Rektorova, I. Gray Matter Changes in Parkinson's and Alzheimer's Disease and Relation to Cognition. *Curr. Neurol. Neurosci. Rep.* **19**, 85-85, doi:10.1007/s11910-019-1006-z (2019).
- 3 Anderson, V. M. et al. Gray matter atrophy rate as a marker of disease progression in AD. *Neurobiol. Aging* **33**, 1194-1202, doi:10.1016/j.neurobiolaging.2010.11.001 (2012).
- 4 Vogt, N. M. et al. Cortical Microstructural Alterations in Mild Cognitive Impairment and Alzheimer's Disease Dementia. *Cereb Cortex* **30**, 2948-2960, doi:10.1093/cercor/bhz286 (2020).
- 5 Sepulcre, J. et al. In Vivo Tau, Amyloid, and Gray Matter Profiles in the Aging Brain. *The Journal of neuroscience : the official journal of the Society for Neuroscience* **36**, 7364-7374, doi:10.1523/JNEUROSCI.0639-16.2016 (2016).
- 6 Li, J., Pan, P., Huang, R. & Shang, H. A meta-analysis of voxel-based morphometry studies of white matter volume alterations in Alzheimer's disease. *Neurosci Biobehav Rev* **36**, 757-763, doi:10.1016/j.neubiorev.2011.12.001 (2012).
- 7 Brun, A. & Englund, E. A white matter disorder in dementia of the Alzheimer type: a pathoanatomical study. *Ann. Neurol.* **19**, 253-262, doi:10.1002/ana.410190306 (1986).
- 8 Araque Caballero, M. Á. et al. White matter diffusion alterations precede symptom onset in autosomal dominant Alzheimer's disease. *Brain* **141**, 3065-3080, doi:10.1093/brain/awy229 (2018).
- 9 Agosta, F. et al. White Matter Damage in Alzheimer Disease and Its Relationship to Gray Matter Atrophy. *Radiology* **258**, 853-863, doi:10.1148/radiol.10101284 (2011).
- 10 Wardlaw, J. M., Valdés Hernández, M. C. & Muñoz-Maniega, S. What are white matter hyperintensities made of? Relevance to vascular cognitive impairment. *J Am Heart Assoc* **4**, 001140-001140, doi:10.1161/JAHA.114.001140 (2015).
- 11 Kandel, B. M. et al. White matter hyperintensities are more highly associated with preclinical Alzheimer's disease than imaging and cognitive markers of neurodegeneration. *Alzheimer's & dementia (Amsterdam, Netherlands)* **4**, 18-27, doi:10.1016/j.dadm.2016.03.001 (2016).
- 12 Kamagata, K. et al. Advanced diffusion magnetic resonance imaging in patients with Alzheimer's and Parkinson's diseases. *Neural Regeneration Research* **15**, 1590-1600, doi:10.4103/1673-5374.276326 (2020).
- 13 Fu, X. et al. Microstructural White Matter Alterations in Mild Cognitive Impairment and Alzheimer's Disease : Study Based on Neurite Orientation Dispersion and Density Imaging (NODDI). *Clin Neuroradiol* **30**, 569-579, doi:10.1007/s00062-019-00805-0 (2020).
- 14 Parker, T. D. et al. Cortical microstructure in young onset Alzheimer's disease using neurite orientation dispersion and density imaging. *Hum Brain Mapp* **39**, 3005-3017, doi:10.1002/hbm.24056 (2018).
- 15 Slattery, C. F. et al. ApoE influences regional white-matter axonal density loss in Alzheimer's disease. *Neurobiol Aging* **57**, 8-17, doi:10.1016/j.neurobiolaging.2017.04.021 (2017).
- 16 Wen, Q. et al. White matter alterations in early-stage Alzheimer's disease: A tract-specific study. *Alzheimers Dement (Amst)* **11**, 576-587, doi:10.1016/j.dadm.2019.06.003 (2019).
- 17 Bartzokis, G. et al. White matter structural integrity in healthy aging adults and patients with Alzheimer disease: a magnetic resonance imaging study. *Arch. Neurol.* **60**, 393-398, doi:10.1001/archneur.60.3.393 (2003).
- 18 Benitez, A. et al. White matter tract integrity metrics reflect the vulnerability of late-myelinating tracts in Alzheimer's disease. *NeuroImage: Clinical* **4**, 64-71, doi:<https://doi.org/10.1016/j.nicl.2013.11.001> (2014).
- 19 Kester, M. I. et al. Associations Between Cerebral Small-Vessel Disease and Alzheimer Disease Pathology as Measured by Cerebrospinal Fluid Biomarkers. *JAMA Neurology* **71**, 855-862, doi:10.1001/jamaneurol.2014.754 (2014).
- 20 Kao, Y.-H., Chou, M.-C., Chen, C.-H. & Yang, Y.-H. White Matter Changes in Patients with Alzheimer's Disease and Associated Factors. *J Clin Med* **8**, 167, doi:10.3390/jcm8020167 (2019).
- 21 Zlokovic, B. V. Neurovascular pathways to neurodegeneration in Alzheimer's disease and other disorders. *Nature Reviews Neuroscience* **12**, 723-738, doi:10.1038/nrn3114 (2011).

- 22 Ujiiie, M., Dickstein, D. L., Carlow, D. A. & Jefferies, W. A. Blood-brain barrier permeability precedes senile plaque formation in an Alzheimer disease model. *Microcirculation* **10**, 463-470, doi:10.1038/sj.mn.7800212 (2003).
- 23 Clifford, P. M. et al. Abeta peptides can enter the brain through a defective blood-brain barrier and bind selectively to neurons. *Brain Res* **1142**, 223-236, doi:10.1016/j.brainres.2007.01.070 (2007).
- 24 Rosenberg, G. A. Blood-Brain Barrier Permeability in Aging and Alzheimer's Disease. *J Prev Alzheimers Dis* **1**, 138-139, doi:10.14283/jpad.2014.25 (2014).
- 25 Clark, L. R. et al. Macrovascular and microvascular cerebral blood flow in adults at risk for Alzheimer's disease. *Alzheimers Dement (Amst)* **7**, 48-55, doi:10.1016/j.dadm.2017.01.002 (2017).
- 26 Asllani, I. et al. Multivariate and univariate analysis of continuous arterial spin labeling perfusion MRI in Alzheimer's disease. *Journal of cerebral blood flow and metabolism : official journal of the International Society of Cerebral Blood Flow and Metabolism* **28**, 725-736, doi:10.1038/sj.jcbfm.9600570 (2008).
- 27 Huang, C.-W. et al. Cerebral Perfusion Insufficiency and Relationships with Cognitive Deficits in Alzheimer's Disease: A Multiparametric Neuroimaging Study. *Scientific reports* **8**, 1541-1541, doi:10.1038/s41598-018-19387-x (2018).
- 28 Berman, S. E. et al. Intracranial Arterial 4D-Flow is Associated with Metrics of Brain Health and Alzheimer's Disease. *Alzheimers Dement (Amst)* **1**, 420-428, doi:10.1016/j.dadm.2015.09.005 (2015).
- 29 Rivera-Rivera, L. A. et al. Changes in intracranial venous blood flow and pulsatility in Alzheimer's disease: A 4D flow MRI study. *J Cereb Blood Flow Metab* **37**, 2149-2158, doi:10.1177/0271678X16661340 (2017).
- 30 Rivera-Rivera, L. A. et al. Intracranial vascular flow oscillations in Alzheimer's disease from 4D flow MRI. *NeuroImage: Clinical* **28**, 102379, doi:<https://doi.org/10.1016/j.nicl.2020.102379> (2020).
- 31 Cermakova, P. et al. Heart failure and Alzheimer's disease. *J Intern Med* **277**, 406-425, doi:10.1111/joim.12287 (2015).
- 32 Thorin, E. Hypertension and Alzheimer disease: another brick in the wall of awareness. *Hypertension* **65**, 36-38, doi:10.1161/hypertensionaha.114.04257 (2015).
- 33 Watts, A. S., Loskutova, N., Burns, J. M. & Johnson, D. K. Metabolic syndrome and cognitive decline in early Alzheimer's disease and healthy older adults. *J Alzheimers Dis* **35**, 253-265, doi:10.3233/jad-121168 (2013).
- 34 Clark, L. R. et al. Association of Cardiovascular and Alzheimer's Disease Risk Factors with Intracranial Arterial Blood Flow in Whites and African Americans. *J Alzheimers Dis* **72**, 919-929, doi:10.3233/jad-190645 (2019).
- 35 Strickland, S. Blood will out: vascular contributions to Alzheimer's disease. *J Clin Invest* **128**, 556-563, doi:10.1172/JCI97509 (2018).
- 36 Johnson, K. M. et al. Improved 3D phase contrast MRI with off-resonance corrected dual echo VIPR. *Magn Reson Med* **60**, 1329-1336, doi:10.1002/mrm.21763 (2008).
- 37 Gu, T. et al. PC VIPR: a high-speed 3D phase-contrast method for flow quantification and high-resolution angiography. *AJNR Am J Neuroradiol* **26**, 743-749 (2005).
- 38 Berman, S. E. et al. Intracranial Arterial 4D Flow in Individuals with Mild Cognitive Impairment is Associated with Cognitive Performance and Amyloid Positivity. *J Alzheimers Dis* **60**, 243-252, doi:10.3233/JAD-170402 (2017).
- 39 Rivera, L. et al. Changes in intracranial venous blood flow and pulsatility in Alzheimer's disease: A 4D flow MRI study. *Journal of Cerebral Blood Flow & Metabolism* **37**, 0271678X16661340-10271678X16661340, doi:10.1177/0271678X16661340 (2016).
- 40 Rivera-Rivera, L. A. et al. 4D flow MRI for intracranial hemodynamics assessment in Alzheimer's disease. *J Cereb Blood Flow Metab* **36**, 1718-1730, doi:10.1177/0271678X15617171 (2016).
- 41 Rivera-Rivera, L. A. et al. Assessment of vascular stiffness in the internal carotid artery proximal to the carotid canal in Alzheimer's disease using pulse wave velocity from low rank reconstructed 4D flow MRI. *Journal of Cerebral Blood Flow & Metabolism*, 0271678X20910302, doi:10.1177/0271678X20910302 (2020).
- 42 Zhang, H., Schneider, T., Wheeler-Kingshott, C. A. & Alexander, D. C. NODDI: practical in vivo neurite orientation dispersion and density imaging of the human brain. *Neuroimage* **61**, 1000-1016, doi:10.1016/j.neuroimage.2012.03.072 (2012).
- 43 Kamiya, K., Hori, M. & Aoki, S. NODDI in clinical research. *Journal of Neuroscience Methods* **346**, 108908, doi:<https://doi.org/10.1016/j.jneumeth.2020.108908> (2020).

- 44 Markl, M., Frydrychowicz, A., Kozerke, S., Hope, M. & Wieben, O. 4D flow MRI. *J Magn Reson Imaging* **36**, 1015-1036, doi:10.1002/jmri.23632 (2012).
- 45 Pelc, N. J., Herfkens, R. J., Shimakawa, A. & Enzmann, D. R. Phase contrast cine magnetic resonance imaging. *Magn. Reson. Q.* **7**, 229-254 (1991).
- 46 Frayne, R. & Rutt, B. K. Understanding acceleration-induced displacement artifacts in phase-contrast MR velocity measurements. *Journal of Magnetic Resonance Imaging* **5**, 207-215, doi:10.1002/jmri.1880050217 (1995).
- 47 Steinman, D. A., Ethier, C. R. & Rutt, B. K. Combined analysis of spatial and velocity displacement artifacts in phase contrast measurements of complex flows. *J Magn Reson Imaging* **7**, 339-346, doi:10.1002/jmri.1880070214 (1997).
- 48 Pelc, N. J., Bernstein, M. A., Shimakawa, A. & Glover, G. H. Encoding strategies for three-direction phase-contrast MR imaging of flow. *Journal of Magnetic Resonance Imaging* **1**, 405-413, doi:<https://doi.org/10.1002/jmri.1880010404> (1991).
- 49 Johnson, K. M. & Markl, M. Improved SNR in phase contrast velocimetry with five-point balanced flow encoding. *Magn Reson Med* **63**, 349-355, doi:10.1002/mrm.22202 (2010).
- 50 Dyverfeldt, P. et al. 4D flow cardiovascular magnetic resonance consensus statement. *J Cardiovasc Magn Reson* **17**, 72, doi:10.1186/s12968-015-0174-5 (2015).
- 51 Bernstein, M. A. & Ikezaki, Y. Comparison of phase-difference and complex-difference processing in phase-contrast MR angiography. *J Magn Reson Imaging* **1**, 725-729, doi:10.1002/jmri.1880010620 (1991).
- 52 Glover, G. H. & Pauly, J. M. Projection reconstruction techniques for reduction of motion effects in MRI. *Magn Reson Med* **28**, 275-289, doi:10.1002/mrm.1910280209 (1992).
- 53 Lustig, M., Donoho, D. & Pauly, J. M. Sparse MRI: The application of compressed sensing for rapid MR imaging. *Magn Reson Med* **58**, 1182-1195, doi:10.1002/mrm.21391 (2007).
- 54 Schrauben, E. M., Anderson, A. G., Johnson, K. M. & Wieben, O. Respiratory-induced venous blood flow effects using flexible retrospective double-gating. *J Magn Reson Imaging* **42**, 211-216, doi:10.1002/jmri.24746 (2015).
- 55 Ma, L. E. et al. Aortic 4D flow MRI in 2 minutes using compressed sensing, respiratory controlled adaptive k-space reordering, and inline reconstruction. *Magn Reson Med* **81**, 3675-3690, doi:10.1002/mrm.27684 (2019).
- 56 Callaghan, F. J., Geddes, L. A., Babbs, C. F. & Bourland, J. D. Relationship between pulse-wave velocity and arterial elasticity. *Med. Biol. Eng. Comput.* **24**, 248-254, doi:10.1007/bf02441620 (1986).
- 57 Nelson, T. R. & Pretorius, D. H. The Doppler signal: where does it come from and what does it mean? *Am J Roentgenol* **151**, 439-447, doi:10.2214/ajr.151.3.439 (1988).
- 58 Grussu, F. et al. Neurite dispersion: a new marker of multiple sclerosis spinal cord pathology? *Annals of Clinical and Translational Neurology* **4**, 663-679, doi:<https://doi.org/10.1002/acn3.445> (2017).
- 59 Zhang, H., Hubbard, P. L., Parker, G. J. & Alexander, D. C. Axon diameter mapping in the presence of orientation dispersion with diffusion MRI. *Neuroimage* **56**, 1301-1315, doi:10.1016/j.neuroimage.2011.01.084 (2011).
- 60 Pruessmann, K. P., Weiger, M., Scheidegger, M. B. & Boesiger, P. SENSE: sensitivity encoding for fast MRI. *Magn Reson Med* **42**, 952-962 (1999).
- 61 Uecker, M. et al. ESPIRiT--an eigenvalue approach to autocalibrating parallel MRI: where SENSE meets GRAPPA. *Magn Reson Med* **71**, 990-1001, doi:10.1002/mrm.24751 (2014).
- 62 Peper, E. S. et al. Regional assessment of carotid artery pulse wave velocity using compressed sensing accelerated high temporal resolution 2D CINE phase contrast cardiovascular magnetic resonance. *Journal of Cardiovascular Magnetic Resonance* **20**, 86, doi:10.1186/s12968-018-0499-y (2018).
- 63 Jimenez, J. E. et al. Feasibility of high spatiotemporal resolution for an abbreviated 3D radial breast MRI protocol. *Magnetic resonance in medicine* **80**, 1452-1466, doi:10.1002/mrm.27137 (2018).
- 64 Bernstein, M. A. et al. Concomitant gradient terms in phase contrast MR: analysis and correction. *Magn Reson Med* **39**, 300-308, doi:10.1002/mrm.1910390218 (1998).
- 65 Loecher, M., Schrauben, E., Johnson, K. M. & Wieben, O. Phase unwrapping in 4D MR flow with a 4D single-step laplacian algorithm. *J Magn Reson Imaging* **43**, 833-842, doi:10.1002/jmri.25045 (2016).
- 66 Schrauben, E. et al. Fast 4D flow MRI intracranial segmentation and quantification in tortuous arteries. *J Magn Reson Imaging* **42**, 1458-1464, doi:10.1002/jmri.24900 (2015).

- 67 Wentland, A. L., Grist, T. M. & Wieben, O. Review of MRI-based measurements of pulse wave velocity: a biomarker of arterial stiffness. *Cardiovasc Diagn Ther* **4**, 193-206, doi:10.3978/j.issn.2223-3652.2014.03.04 (2014).
- 68 Jenkinson, M., Beckmann, C. F., Behrens, T. E., Woolrich, M. W. & Smith, S. M. FSL. *Neuroimage* **62**, 782-790, doi:10.1016/j.neuroimage.2011.09.015 (2012).
- 69 Tournier, J. D. *et al.* MRtrix3: A fast, flexible and open software framework for medical image processing and visualisation. *Neuroimage* **202**, 116137, doi:10.1016/j.neuroimage.2019.116137 (2019).
- 70 Veraart, J. *et al.* Denoising of diffusion MRI using random matrix theory. *Neuroimage* **142**, 394-406, doi:10.1016/j.neuroimage.2016.08.016 (2016).
- 71 Kellner, E., Dhital, B., Kiselev, V. G. & Reisert, M. Gibbs-ringing artifact removal based on local subvoxel-shifts. *Magn Reson Med* **76**, 1574-1581, doi:10.1002/mrm.26054 (2016).
- 72 Smith, S. M. Fast robust automated brain extraction. *Hum Brain Mapp* **17**, 143-155, doi:10.1002/hbm.10062 (2002).
- 73 Andersson, J. L. R. & Sotiroopoulos, S. N. An integrated approach to correction for off-resonance effects and subject movement in diffusion MR imaging. *Neuroimage* **125**, 1063-1078, doi:10.1016/j.neuroimage.2015.10.019 (2016).
- 74 Bastiani, M. *et al.* Automated quality control for within and between studies diffusion MRI data using a non-parametric framework for movement and distortion correction. *Neuroimage* **184**, 801-812, doi:10.1016/j.neuroimage.2018.09.073 (2019).
- 75 Andersson, J. L. R., Graham, M. S., Zsoldos, E. & Sotiroopoulos, S. N. Incorporating outlier detection and replacement into a non-parametric framework for movement and distortion correction of diffusion MR images. *Neuroimage* **141**, 556-572, doi:10.1016/j.neuroimage.2016.06.058 (2016).
- 76 Bassar, P. J., Mattiello, J. & LeBihan, D. Estimation of the effective self-diffusion tensor from the NMR spin echo. *J. Magn. Reson. B* **103**, 247-254, doi:10.1006/jmrb.1994.1037 (1994).
- 77 Smith, S. M. *et al.* Tract-based spatial statistics: voxelwise analysis of multi-subject diffusion data. *Neuroimage* **31**, 1487-1505, doi:10.1016/j.neuroimage.2006.02.024 (2006).
- 78 Andersson, J., Jenkinson, M. & Smith, S. Non-linear registration, aka spatial normalisation. (2010).
- 79 Ho, D., Imai, K., King, G. & Stuart, E. A. MatchIt: Nonparametric Preprocessing for Parametric Causal Inference. *2011* **42**, 28, doi:10.18637/jss.v042.i08 (2011).
- 80 Woolrich, M. W., Behrens, T. E., Beckmann, C. F., Jenkinson, M. & Smith, S. M. Multilevel linear modelling for fMRI group analysis using Bayesian inference. *Neuroimage* **21**, 1732-1747, doi:10.1016/j.neuroimage.2003.12.023 (2004).
- 81 Winkler, A. M., Ridgway, G. R., Webster, M. A., Smith, S. M. & Nichols, T. E. Permutation inference for the general linear model. *Neuroimage* **92**, 381-397, doi:10.1016/j.neuroimage.2014.01.060 (2014).
- 82 Román, G. C. Vascular dementia may be the most common form of dementia in the elderly. *J Neurol Sci* **203-204**, 7-10, doi:10.1016/s0022-5110(02)00252-6 (2002).
- 83 Guerrero, J. M., Adluru, M., Kecskemeti, S., Davidson, R. J. & Alexander, A. L. in *ISMRM*.
- 84 Zhang, Y. *et al.* Atlas-guided tract reconstruction for automated and comprehensive examination of the white matter anatomy. *Neuroimage* **52**, 1289-1301, doi:10.1016/j.neuroimage.2010.05.049 (2010).
- 85 Ressel, V., van Hedel, H. J. A., Scheer, I. & O'Gorman Tuura, R. Comparison of DTI analysis methods for clinical research: influence of pre-processing and tract selection methods. *Eur Radiol Exp* **2**, 33-33, doi:10.1186/s41747-018-0066-1 (2018).
- 86 Schöll, M. *et al.* PET Imaging of Tau Deposition in the Aging Human Brain. *Neuron* **89**, 971-982, doi:10.1016/j.neuron.2016.01.028 (2016).
- 87 Thal, D. R., Attems, J. & Ewers, M. Spreading of amyloid, tau, and microvascular pathology in Alzheimer's disease: findings from neuropathological and neuroimaging studies. *J Alzheimers Dis Suppl* **4**, S421-429, doi:10.3233/jad-141461 (2014).
- 88 Colgan, N. *et al.* Application of neurite orientation dispersion and density imaging (NODDI) to a tau pathology model of Alzheimer's disease. *Neuroimage* **125**, 739-744, doi:10.1016/j.neuroimage.2015.10.043 (2016).

Appendix:

